

Persistent homology elucidates hierarchical structures in amorphous solids responsible for mechanical properties

Emi Minamitani*^{1,2}, Takenobu Nakamura³, Ippei Obayashi⁴, Hideyuki Mizuno⁵

1. SANKEN, Osaka University, 8-1 Mihogaoka, Ibaraki, Osaka 567-0047, Japan
2. JST, PRESTO, 4-1-8 Honcho, Kawaguchi, Saitama 332-0012, Japan
3. National Institute of Advanced Industrial Science and Technology (AIST), 1-1-1 Umezono, Tsukuba, Ibaraki 305-8568, Japan
4. Center for Artificial Intelligence and Mathematical Data Science, Okayama University, Okayama 700-8530, Japan
5. Graduate School of Arts and Sciences, The University of Tokyo, Tokyo 153-8902, Japan

Abstract

Understanding the role of atomic-level structures in determining amorphous material properties has been a long-standing challenge in solid-state physics. Upon mechanical loading, amorphous materials undergo both simple affine displacement and spatially inhomogeneous non-affine displacement. These two types of displacement contribute differently to the elastic modulus, i.e., the Born (or affine) and non-affine terms. Whether “soft” local structures characterized by either small Born terms or large non-affine displacements differ has remained an unanswered question despite the importance in fundamental and applied physics. To address this question, we combined molecular dynamics simulations and persistent homology analyses for amorphous Si. We found that the characteristics of local structures with large non-affine displacements differed significantly from those with small Born terms. The local structures surrounding atoms with small Born terms are characterized at the scale of short-range order (SRO), whereas those surrounding atoms with large non-affine displacements have hierarchical structures ranging from SRO to medium-range order. Furthermore, we found that these hierarchical structures are related to low-energy localized vibrational excitations. The correlation between the non-affine displacement and hierarchical geometric features elucidated by persistent homology provides a new viewpoint for understanding and designing the mechanical properties of amorphous materials based on their static structures.

Introduction

The correlation between the structure and properties of amorphous materials has long been a mystery in materials science, even for the fundamental mechanical properties. In crystals, defects and dislocations respond to strain, determining the stress distribution and resulting deformation. However, these crystalline definitions cannot be directly applied to the disordered and nonperiodic structures of amorphous materials. There is still debate over whether certain local structures within amorphous materials play a role in mechanical responses, such as defects and dislocations in crystals.¹

A significant difference between the strain response of amorphous materials and that of crystals is the non-affinity of atomic displacements.²⁻⁵ When strain is applied to amorphous materials, spatially inhomogeneous atomic displacements, known as non-affine displacements, occur in addition to affine displacements, which simply follows the imposed strain. Thus, the mechanical response can be decomposed into components arising from both types of displacement. For the elastic moduli, the effects derived from the former are referred to as the non-affine term, whereas those from the latter are referred to as the Born term.^{2,3,6} Because these Born and non-affine terms contribute to the total elastic modulus in the same order of magnitude, it is necessary to understand both terms. The overall elastic modulus can be determined by the value obtained by subtracting the non-affine term from the Born term. Therefore, “soft” structures that easily respond to strain and reduce the elastic modulus constitute regions where the Born term is small and/or the non-affine displacement is large.

Several studies have addressed the characteristics of soft local structures in amorphous materials. Demkowicz and Argon evaluated whether the local environment of atoms is more liquid- or solid-like based on the average and standard deviation of the interatomic angles; they demonstrated their correlations with the shear modulus.^{7,8} Falk and colleagues related the concept of shear transformation zones,⁹ where atomic rearrangement occurs under shear strain, to non-affine displacement by using atomistic simulation.^{10,11} Additionally, the flexibility volume, which is defined as the product of the Voronoi volume and mean squared displacement, has been demonstrated to be strongly correlated with the shear modulus.^{12,13} Alternatively, machine learning models that use structural information as input have been widely applied to identify soft regions.¹⁴⁻¹⁶ Although these previous studies indicate that certain soft local structures exist and are strongly correlated with mechanical responses, we have not yet identified specific local structures.

To address this issue, we have applied persistent homology,^{17,18} a representative technique of topological data analysis, to extract the structural features of amorphous materials and identify the missing link between local structures and mechanical properties. A typical feature of amorphous materials is the medium-range order (MRO).¹⁹ The presence of MRO is believed to affect various properties. However, the number of atoms constituting the structures corresponding to MRO spans a wide scale, ranging from tens to hundreds, making the effect of MRO difficult to understand by using conventional structural analysis methods. Persistent homology, a multiscale analysis method, can solve this problem.

Persistent homology is based on a mathematical topology. Mathematically, a set combined with a topology is treated as a topological space. Topological spaces are characterized by n -dimensional holes, which can be represented by homology groups. When defining a set of points by using atomic coordinates, it is natural to introduce a topology based on the presence or absence of bonds between the atoms. As the threshold for determining whether a bond exists between the atoms changes, the topology also changes. This process is illustrated in Figure 1. To demonstrate the change of the threshold of bond formation, a sphere is placed at each atom and the radius of the sphere gradually increases. When the spheres make contact, a bond is established between the atoms. As the radius increases, the number of bonds increases, and a ring is formed. This ring corresponds to the presence of a one-dimensional hole in the topological space and is termed a “cycle.” As the radius continues to increase, the ring becomes covered with spheres. At this point, the cycle is considered to have transformed into a “boundary,” which corresponds to the edge of a filled polygon. Because homology groups are defined as the quotient group of cycles by boundaries, the transformation from cycles to boundaries is fundamentally important.

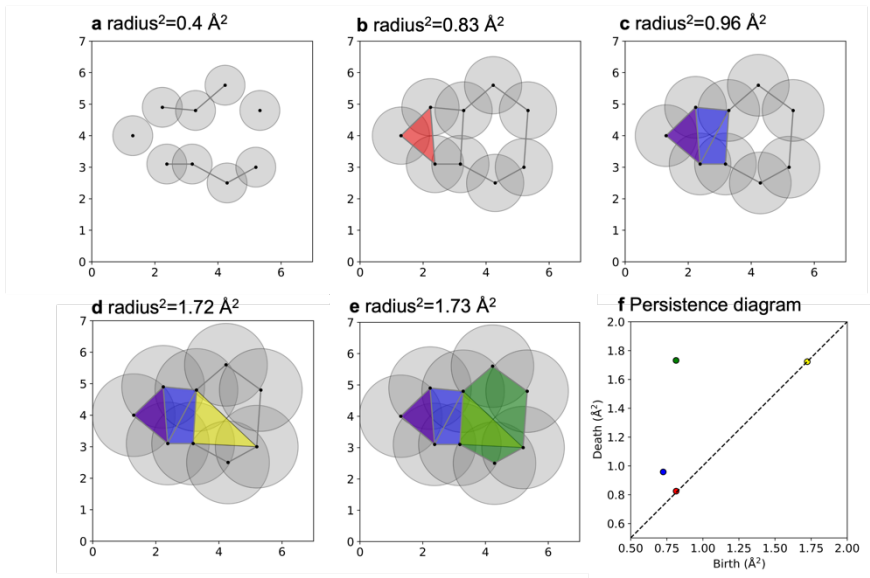


Figure 1. Illustration of persistent homology method. **a–d** Filtration process. The filled polygons denote cycles transforming into boundaries. The growing sequence of the empty and filled polygons also depicts the concept of children, which systematize the hierarchical relationships in persistent homology. The red triangle is a child of the blue pentagon, and the yellow triangle is a child of the green hexagon. **f** Resulting persistence diagram derived from the filtration process. We employed the squared values of the radii of the spheres used in the filtration procedure as the birth and death radii. Therefore, their units are \AA^2 . The colors of the points in the diagram correspond to the polygons of the same color.

Therefore, persistent homology describes the topological features of atomic structures by using pairs of radii of spheres at which new cycles are born (birth radius) and radii at which these cycles transform into boundaries (death radius). The scatter plot for the pairs of birth and death radii (birth–death pair) is called a persistence diagram, as shown in Figure 1f. Based on the above definitions, persistent homology has the advantage of simultaneously capturing structural features at various scales. This feature has been applied to elucidate structures and structure–property correlations in disordered materials.^{20–33}

Furthermore, the use of persistent homology allows us to investigate the hierarchical nature of structural features. During the transformation of a cycle into a boundary, smaller cycles are formed and transformed into boundaries within that cycle. Two examples of these cycles are shown in Figure 1. The red triangle is born at a squared radius of 0.82\AA^2 and dies at a squared radius of 0.83\AA^2 . This birth–death interval of the red triangle is within that of the blue pentagon,

which is born at a squared radius of 0.72 \AA^2 and dies at a squared radius of 0.96 \AA^2 . Similarly, the yellow triangle is born and dies within the birth–death interval of the green hexagon. In this paper, we refer to these smaller inner cycles as children. Note that this concept is referred to as a secondary ring in other reports.²⁰ Children occur in systems with corner-, edge-, and face-sharing units, such as covalent glass, reflecting the hierarchical nature of the structure.²⁰

In this study, we analyzed the shear modulus of amorphous Si by using molecular dynamics simulations in combination with persistent homology analysis. We found that the characteristics of local structures with large non-affine displacements differ from those of structures with small Born terms. The local structures surrounding atoms with small Born terms were found to consist of small rings with relatively few vertices. In addition, these rings were found to not contain children and be characterized by short-range order (SRO) instead of MRO. In contrast, the local structures surrounding atoms with large non-affine displacements were found to consist of relatively large rings with more vertices than those with small Born terms. Furthermore, these rings were found to contain children and make up parts of hierarchical structures ranging from SRO to MRO on multiple scales. It is also shown that atoms with large non-affine displacements correspond to atoms with large amplitudes of low-energy localized vibrational excitations.

These analyses clearly demonstrate that there are two different types of “soft” regions in amorphous materials. Particularly, regions with small Born terms can be understood as areas with disorder in bond-length and bond-angle distribution on the scale of SRO, whereas regions with large non-affine displacements require a different explanation. Regions with large non-affine displacements are locations where low-energy localized modes occur, and realizing such vibrational modes requires not only simple disorder, but also constraints from the hierarchical structures constituted by MRO. The correlation between non-affine displacements and hierarchical geometric features elucidated by persistent homology provides a new viewpoint for understanding and designing mechanical responses in amorphous materials based on their static structure.

Results

Born term and non-affine displacement

First, we evaluated the correlation between the Born term and non-affine displacement with shear strain. Figure 2a shows the scatter plot of the Born term $C_{i,\alpha\beta\kappa\chi}^{born}$ and non-affine displacement $D_{i,\alpha\beta}^{NA}$ for each atom in the amorphous Si structure depicted in Figure 2b. The Greek subscripts of $C_{i,\alpha\beta\kappa\chi}^{born}$

and $D_{i,\alpha\beta}^{NA}$ specify the directions x, y , or z . For the Born term, we use the calculated value of $B_i = (C_{i,xyxy}^{Born} + C_{i,yzyz}^{born} + C_{i,zzzx}^{born})/3$; for the non-affine displacement, we use the calculated value of $D_i = (|D_{i,xy}^{NA}| + |D_{i,yz}^{NA}| + |D_{i,zx}^{NA}|)/3$.

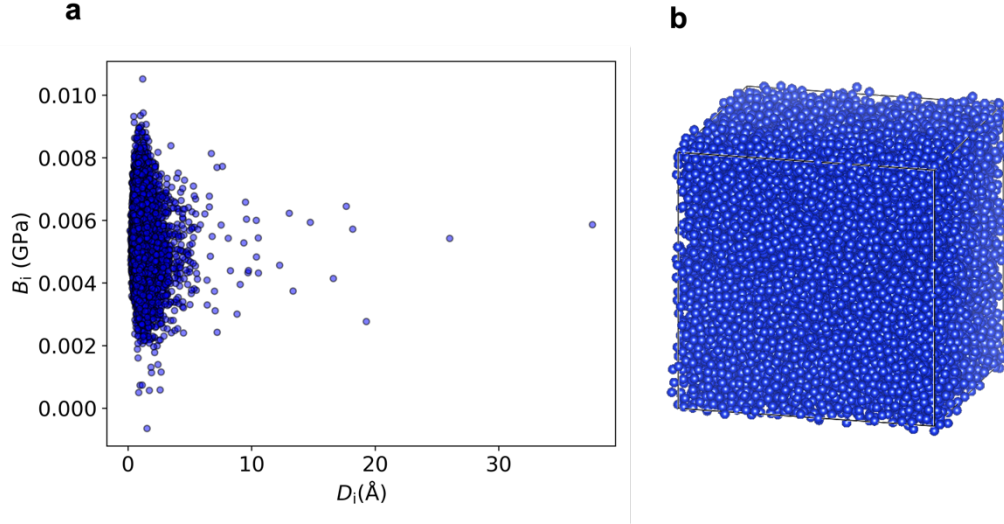


Figure 2. Calculated Born term (B_i) and non-affine displacement (D_i) results for each atom in amorphous Si. **a** Scatter plot of D_i and B_i . **b** Amorphous structure comprising 13,824 Si atoms used for the analysis.

Figure 2a shows that there was no clear correlation between the Born term and non-affine displacement. Particularly, atoms with large non-affine displacements were generally not found to be associated with small Born terms. This suggests that the “soft” local structures identified based on small Born terms may differ from those with large non-affine displacements. For further analysis, we focused on 10 atoms with the largest Born terms (B_{max10}), 10 atoms with the smallest Born terms (B_{min10}), and 10 atoms with the largest non-affine displacements (NA_{max10}).

Differences in persistence diagrams

The persistence diagram highlights the distinct local structural features that correlate with the Born terms and non-affine displacements. Figure 3a shows a persistence diagram that was obtained by using the atomic coordinates of the sample depicted in Figure 2b. In Figure 3a, owing to the vast number of birth–death pairs, the data were processed as a two-dimensional histogram. The atomic rings corresponding to each birth–death pair in the persistence diagram were identified

by performing inverse analysis. We analyzed the ring structures corresponding to all birth–death pairs within the interval $[0, 5]$ for birth and death radii and determined the cycles that included Bmax10, Bmin10, and NAmx10. The scatter plot of the birth–death pairs for each of these groups is shown in Figure 3b–d.

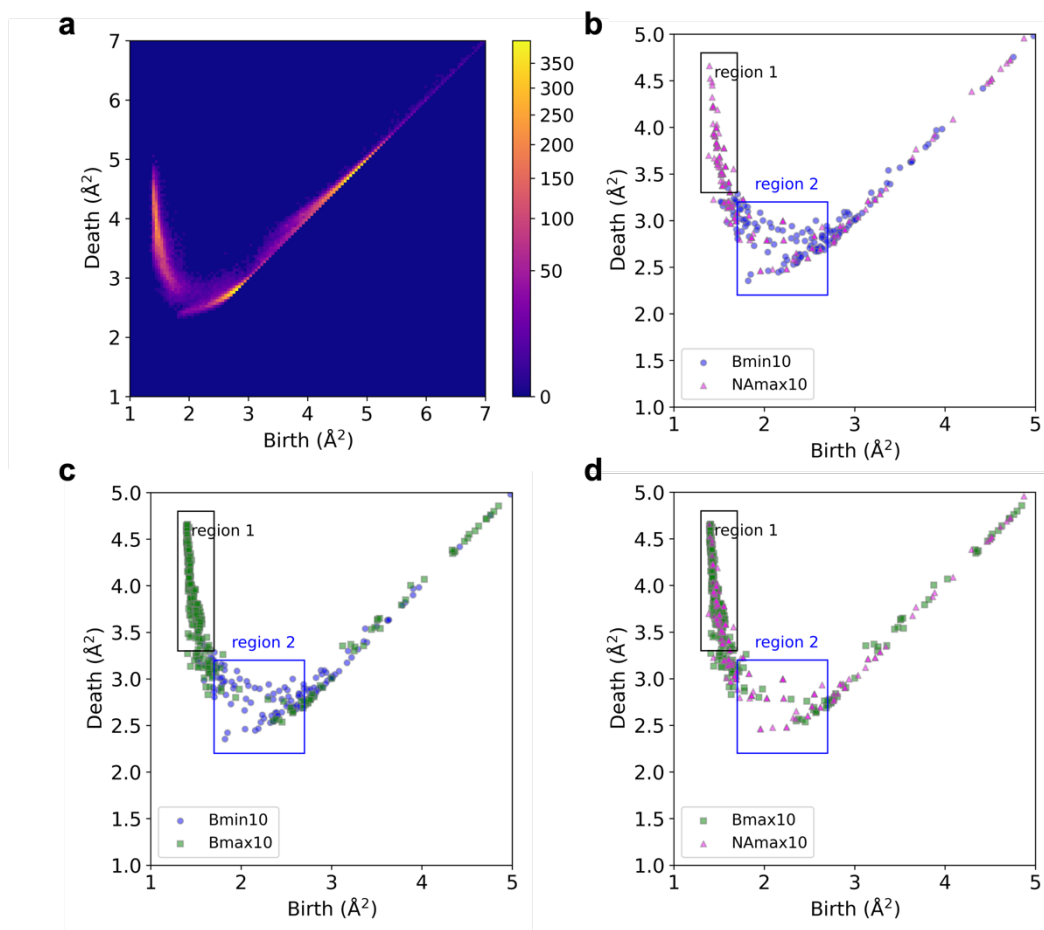


Figure 3. Persistence diagram and birth–death pair distributions. **a** Persistence diagram derived from the structure in Figure 2b. **b** Distribution of birth–death pairs for cycles including Bmin10 and NAmx10; **c** Bmin10 and Bmax10; and **d** Bmax10 and NAmx10. The black square indicates the range of Region 1, and the blue square indicates the range of Region 2.

The distribution of birth–death pairs differed significantly between the cycles for Bmin10 and NAmx10. This clearly indicated that the structural features captured by persistent homology differed between the two groups. Although the distribution of cycles for Bmin10 also differed from that of cycles for Bmax10, the distribution of cycles for Bmax10 was similar to that of cycles for NAmx10. For the cycles corresponding to Bmax10 and NAmx10, the birth–death pairs were

respectively concentrated in the intervals $[1.3, 1.7]$ and $[3.3, 4.8]$ for the birth and death radii (Region 1), whereas there were fewer birth–death pairs in the intervals $[1.7, 2.2]$ and $[2.7, 3.2]$ for the birth and death radii, respectively (Region 2). The cycles for Bmin10 exhibited the opposite trend. As shown in Figure S1, similar trends were observed in the results obtained for the 10 different samples. Thus, we have concluded that Bmax10 and NA max10 have similar structural features, whereas Bmin10 yielded a different persistence diagram.

Differences in local structures

To confirm the relationship between the distribution of the birth–death pairs and local structures, we visualized the structures corresponding to the cycles for Bmax10, NAmx10, and Bmin10 by conducting inverse analysis. The results are shown in Figure 4.

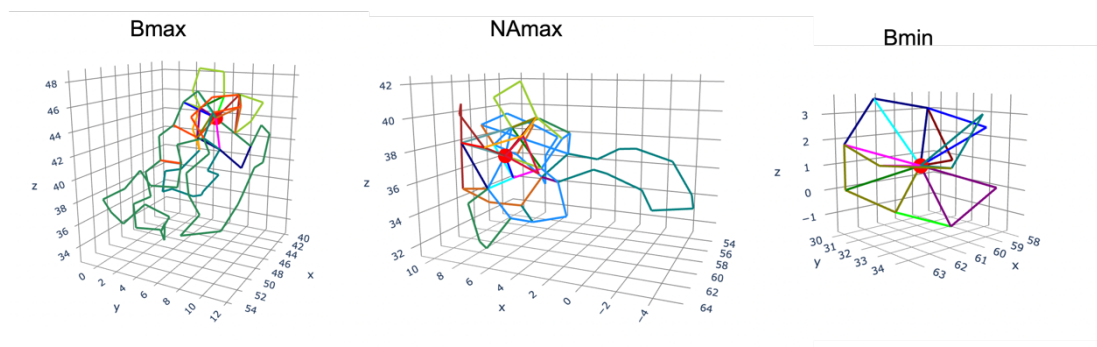


Figure 4. Visualizations of the structures corresponding to the cycles that respectively include the atom with the largest Born term (Bmax), largest non-affine displacement (NAmax), and smallest Born term (Bmin). The position of each specified atom is marked by a red sphere. The color of the polygons indicates the corresponding cycle.

Figure 4 shows the structures corresponding to the cycles that respectively include the atom with the largest Born term (Bmax), largest non-affine displacement (NAmax), and smallest Born term (Bmin). The group of cycles including atoms with large Born terms and large non-affine displacements had large ring structures with numerous vertices, corresponding to the birth–death pairs with large death radii. In contrast, cycles that contained atoms with small Born terms tended to be composed of small triangles.

To confirm the generality of the above-mentioned results, we identified the structures corresponding to the cycles for NAmx10, Bmax10, and Bmin10 for 10 different samples and

constructed histograms of their vertex counts, as shown in Figure 5a. The vertex count reached 700, but Figure 5 only shows a range of 3–200. As is evident from this figure, the cycles for Bmin10 tended to have significantly fewer vertices than those for NAmx10 and Bmax10.

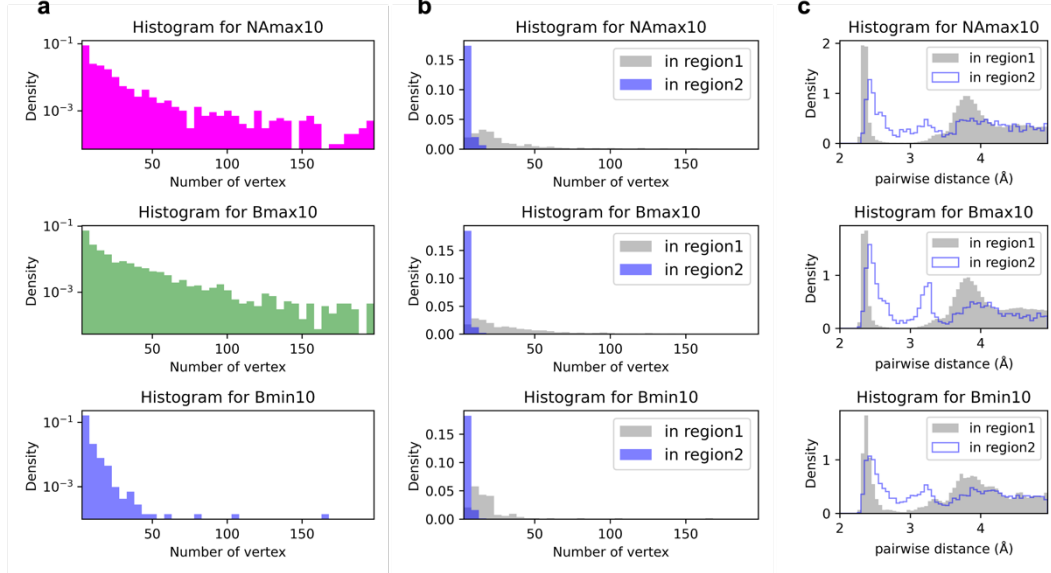


Figure 5. Results of the analysis of number of vertices. **a** Histograms of vertex counts in ring structures corresponding to cycles for NAmx10, Bmax10, and Bmin10 for 10 samples. **b** Histograms of vertex counts restricted to birth–death pairs within Regions 1 and 2. **c** Histograms of pairwise distances within ring structures corresponding to birth–death pairs within Regions 1 and 2.

Furthermore, when analyzing the vertex counts restricted to birth–death pairs within Regions 1 and 2, as shown in Figure 5b, we found that the trends in these two regions differ significantly. The vertex counts for cycles corresponding to birth–death pairs in Region 2 were very small, whereas those in Region 1 exhibited a long-tail distribution. In addition, we analyzed the distribution of pairwise distances within cycles in each region. As shown in Figure 5c, the histogram of the pairwise distances in Region 1 revealed a sharp first peak and a clear second peak near 3.8 Å, corresponding to small-scale MRO. (The position of this second peak matched the death radius distribution in Region 1. When the death radius was 4.0 \AA^2 , the radius of spheres in the filtration was 2.0 Å, resulting in an interatomic pairwise distance of 4.0 Å.) In contrast, the histogram in Region 2 shows a broad first peak and an additional peak near 3.2 Å, which is absent in Region 1. The presence of this additional peak indicates short-range disorder in the bond length and angles that break the MRO. Considering these results, we conclude that the birth–death pairs in Region 2 correspond to structures with short-range disorder, whereas those in Region 1

correspond to MRO structures. Similar distributions of birth–death pairs and their correlations with short-range disorders and MRO formation have previously been reported.²⁷

Statistical analysis of these 10 samples revealed that 61.7% and 12.0% of the cycles for Bmax10 had birth–death pairs in Regions 1 and 2, respectively. For NAmx10, the proportions were 51.1% and 17.2%, respectively; alternatively, for Bmin10, they were 7.4% and 45.1%, respectively. This indicates that the local environment surrounding the atoms associated with large Born terms has less short-range disorder and well-developed MRO. Conversely, the local environment surrounding atoms associated with small Born terms exhibited more short-range disorder and suppressed MRO. The local environment surrounding atoms with large non-affine displacements was similar to that corresponding to atoms associated with a large Born term. However, the larger ratio of the birth–death pairs in Region 2 indicates that these atoms exhibited unique local structures in which short-range disorder and MRO coexist.

It should be noted that such characteristics cannot be captured by conventional local structural indicators, such as the Voronoi volume and interatomic angle. As shown in Figure S2, the Voronoi volume of each atom had no correlation with the non-affine displacement, and only a weak correlation with the Born term. In the scatter plot of the average and standard deviation of the interatomic angles, proposed by Demkowicz and Argon as an indicator of the atomic environment,⁸ Bmax10 was concentrated in specific regions. Therefore, the characteristics of the atoms associated with large Born terms were captured by using this indicator. In contrast, NAmx10 and Bmin10 were distributed across various locations, exhibiting no clear features. The respective relationships between the local environments of atoms with large non-affine displacements and the SRO, MRO, and corresponding hierarchical structures can only be elucidated by applying persistent homology for multiscale analysis, which was indeed achieved in this study.

Analysis of children

We also examined the hierarchical structural characteristics that were extracted via persistent homology. As shown in Figure 5a and b, a characteristic of the groups of cycles for Bmax10 and NAmx10 is not only the presence of large cycles with many vertices, but also the nested structure of smaller cycles within the larger ones. The presence or absence of such nested structures can be quantitatively evaluated by applying persistent homology to analyze children.

Figure 6a–c show the distributions of birth–death pairs for cycles for Bmax10, NAmx10, and

Bmin10 according to the presence/absence of children. For Bmax10 and NAmx10, the birth–death pairs in Region 1 possessed children. Additionally, as shown in Figure 6d–e, for Bmax10 and NAmx10, the cycles in Region 2 were children of larger cycles in the same group that included the same atom. Particularly, for NAmx10, the finite number of birth–death pairs in Region 2 suggests that the local structures surrounding atoms with large non-affine displacements have a hierarchical structure corresponding to MRO structure involving short-range disorder. In contrast, such a hierarchical structure that correlates the short-range scale with MRO was not observed for Bmin10-related cycles.

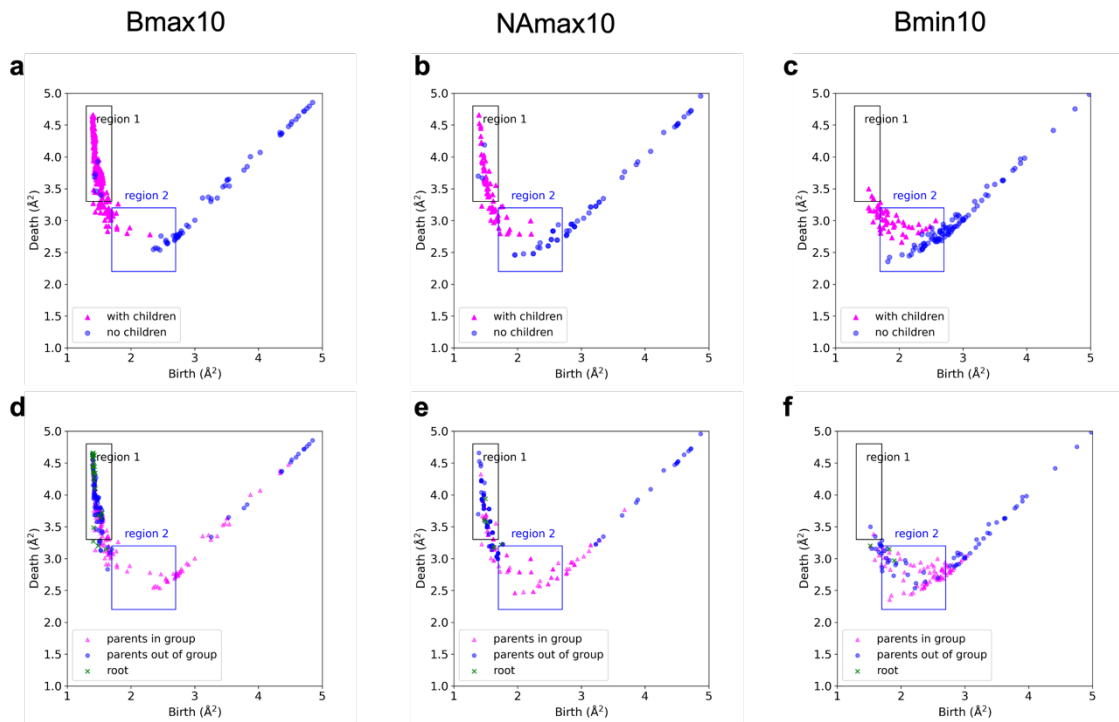


Figure 6. Results of analyses for the children. **a–c** Presence/absence of children in cycles for Bmax10, NAmx10, and Bmin10. **d–f** Results of plotting the persistence diagram with different colors to indicate whether the parent cycle is part of the same group of cycles that include the same atom. In **d–f**, “root” indicates cycles that do not have parents.

To confirm the generality of the above-mentioned results, we applied a similar analysis to 10 different samples and plotted histograms of the number of children and cycles in Regions 1 and 2 (Figure 7). Similar to the trends for the vertex counts, the cycles for NAmx10 and Bmax10 resulted in long-tailed distributions for the number of children; alternatively, the cycles for Bmin10 had fewer children. Additionally, it is evident that the number of children per cycle in

Region 2 was significantly less than that in Region 1. Statistical analysis of these 10 samples revealed that 91.9% of the cycles for NAm₁₀ in Region 2 were children of larger cycles for NAm₁₀, generally indicating the presence of a hierarchical structure.

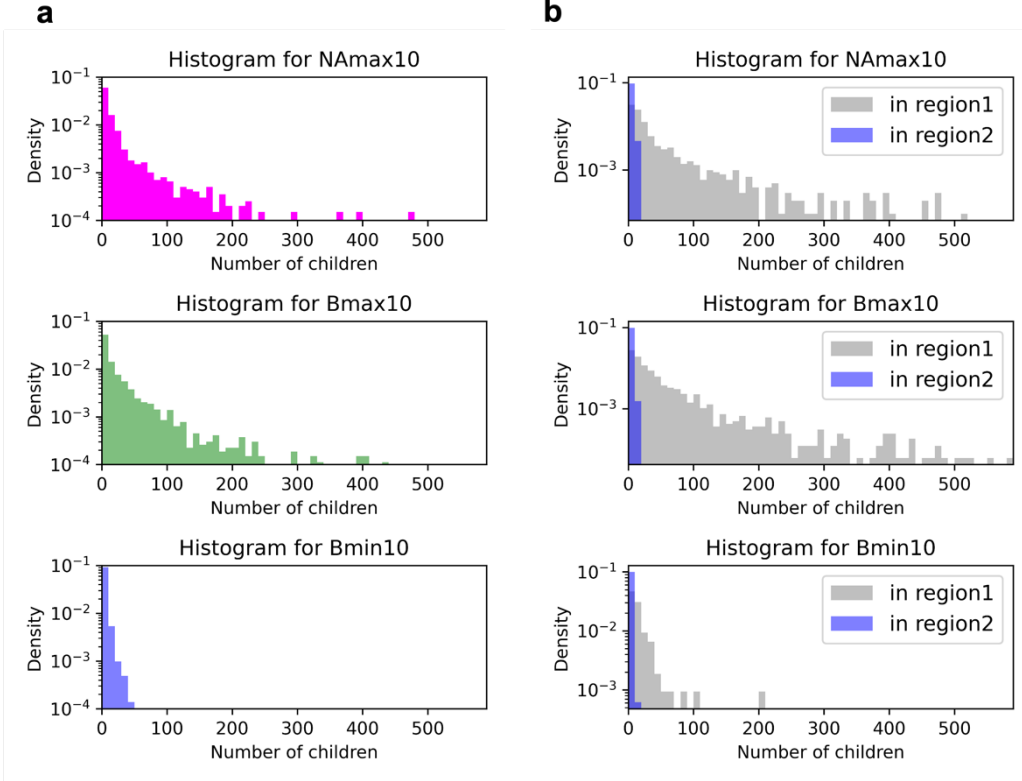


Figure 7. Results of statistical analyses for number of children for 10 samples. **a** Histograms of the number of children for cycles for NAm₁₀, Bmax₁₀, and Bmin₁₀. **b** Corresponding histograms of the number of children restricted to cycles with birth–death pairs in Regions 1 and 2.

Correlation with low-energy localized vibrational excitations

The non-affine displacement can be decomposed by the eigenvectors of vibrational mode, ψ_p , as shown in Equation (12) in the Methods section. This suggests that the non-affine displacement is strongly correlated with the amplitude of the eigenvectors of the vibrational modes. Given that the frequency of the vibrational modes appears in the denominator, it is expected that the non-affine displacement is determined by the low-energy localized vibrational modes. To confirm this, we investigated the localization of the vibrational modes. For modes with strong localization, we analyzed the correlation between their amplitude and non-affine displacement, as well as the Born

term. In addition, we examined whether the cycles for Bmax10, Bmin10, and NAmx10 overlapped with the distribution of low-energy localized modes. Figure 8a shows the results of calculating the inversion participation ratio (IPR) for 1000 low-energy vibrational modes. The IPR is defined as follows:

$$IPR(p) = N_{atom} \sum_i^{N_{atom}} (\psi_{p_{ix}})^4 + (\psi_{p_{iy}})^4 + (\psi_{p_{iz}})^4, (1)$$

where $\psi_{p_{ix}}$, $\psi_{p_{iy}}$, and $\psi_{p_{iz}}$ denote the x, y, and z components of the p -th eigenvector $\boldsymbol{\psi}_p$ for atom i .

A higher IPR value indicates greater localization. We selected low-energy localized modes with IPR values above 50 and calculated the amplitudes of the low-energy localized modes for each atom by using their eigenvectors, as follows:

$$AMP_i = \sum_p^{loc} \frac{1}{\lambda_p} (|\psi_{p_{ix}}| + |\psi_{p_{iy}}| + |\psi_{p_{iz}}|). (2)$$

The superscript *loc* in Equation (2) indicates the summation over the low-energy localized modes. As shown in Figure 8b and c, although the non-affine displacement of each atom was strongly correlated with AMP_i , such a correlation was not observed with the Born term. Additionally, as shown in Figure 8d, the distribution of AMP_i within cycles for Bmax10, Bmin10, and NAmx10 demonstrates that only cycles for NAmx10 have a strong spatial overlap with regions of large amplitudes of low-energy localized modes.

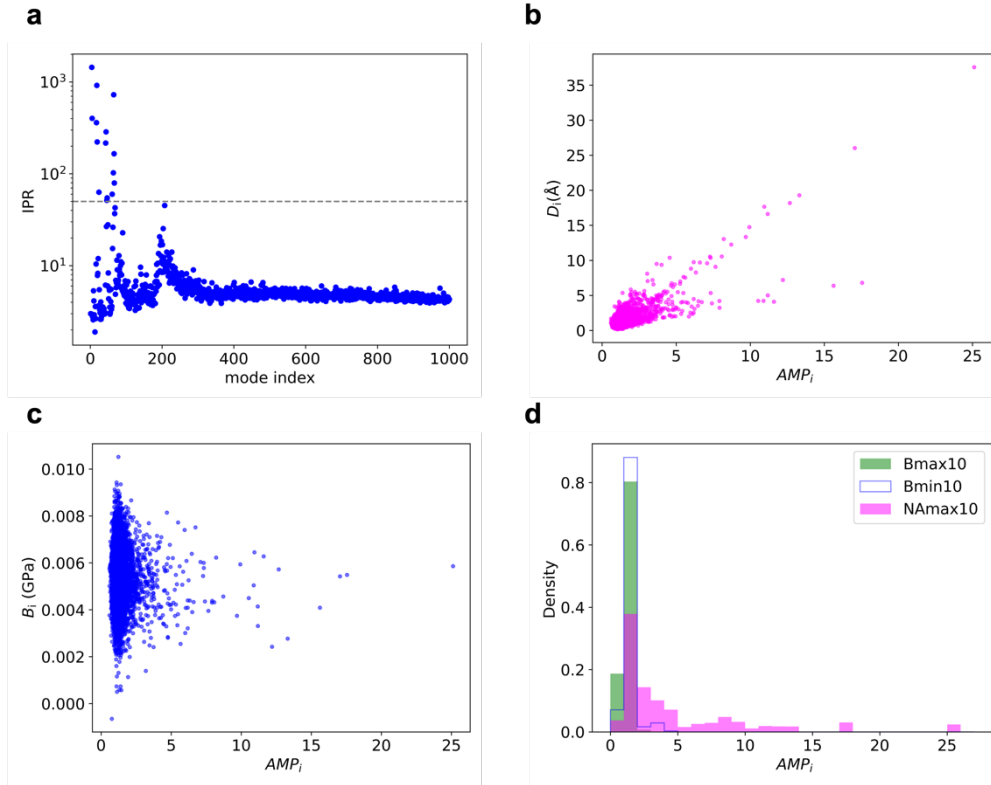


Figure 8. Low-energy localized mode results. **a** IPR results. **b** D_i as a function of AMP_i . **c** B_i as a function of AMP_i . **d** Histograms of AMP_i values for the cycles for Bmax10, Bmin10, and NAmx10.

Considering the results presented thus far, we can conclude that the hierarchical structure that characterizes the local environment surrounding NAmx10, where short-range disorder coexists with MRO, promotes the emergence of low-energy localized modes, leading to large non-affine displacements.

Discussion

In this study, by focusing on the shear modulus of amorphous Si, we combined molecular dynamics simulations and persistent homology analysis to reveal that the characteristics of local structures with small Born terms significantly differ from those with large non-affine displacements. The local structures surrounding the atoms associated with small Born terms consisted of small rings with relatively few vertices. In contrast, the local structures surrounding atoms with large non-affine displacements consisted of larger rings with more vertices.

A local structure with a large Born term is also characterized by the presence of larger rings with more vertices. However, the hierarchy within these structures were found to differ from that within a local structure with a large non-affine displacement. Persistence diagram-based analysis of the nested structures revealed that short-range disorder is more significant in regions with large non-affine displacement than in regions with large Born terms. Thus, the coexistence of short-range disorder and MRO characterizes regions with large non-affine displacement. In addition, the distribution of atoms with large non-affine displacements was found to overlap with the distribution of low-energy localized vibrational modes, suggesting that the hierarchical structure surrounding the atoms associated with large non-affine displacement is also related to the emergence of low-energy localized modes.

The correlation between the hierarchical structures described here and the corresponding mechanical responses has been elucidated through the application of persistent homology, as this insight is generally difficult to obtain by using standard structural indicators such as the Voronoi volume or interatomic angle. Notably, we focused on amorphous Si as the target material, but similar hierarchical structures exist in other materials, such as SiO₂ and Cu-Zr metallic glasses.²⁰ Therefore, our analysis is expected to be broadly applicable to as a tool to facilitate understanding of the mechanical responses of various amorphous and glassy materials.

Although this study focused on the elastic moduli, the approach can be extended to plastic deformation. Identifying the regions in which plastic deformation occurs is a challenging problem that has been widely debated among various researchers.³⁴⁻⁴⁷ Many of the previous studies were designed to obtain an understanding of plastic events within an energy-landscape framework. In this framework, the regions in which plastic events occur, which are often referred to as soft spots or defects, are identified in terms of low-energy localized modes,^{34-37,41,43,44} nonlinear energy excitations,^{38,39} instantaneous normal modes,⁴¹⁻⁴³ and non-affine displacement fields.⁴⁰ Our persistent homology approach can extract structural characteristics in regions where localized excitations and large non-affine displacements occur, and it can also be applied to identify locations of plastic deformation. Therefore, our findings open up new avenues for future research in understanding and designing the mechanical responses of amorphous materials based on their static structures.

Methods

Elastic moduli and non-affine displacement in amorphous materials

The elastic constant $C_{\alpha\beta\kappa\chi}$ in amorphous materials can be defined by using the Born term $C_{\alpha\beta\kappa\chi}^{Born}$ and non-affine term $C_{\alpha\beta\kappa\chi}^{NA}$, as follows³:

$$C_{\alpha\beta\kappa\chi} = C_{\alpha\beta\kappa\chi}^{Born} - C_{\alpha\beta\kappa\chi}^{NA}, \quad (3)$$

where

$$C_{\alpha\beta\kappa\chi}^{Born} = \frac{1}{V} \frac{\partial^2 U}{\partial \eta_{\alpha\beta} \partial \eta_{\kappa\chi}}, \quad (4)$$

and

$$C_{\alpha\beta\kappa\chi}^{NA} = \sum_i \sum_{j \neq i} \frac{1}{V} \Xi_{\alpha\beta}^i (H^{-1})_{ij} \Xi_{\kappa\chi}^j. \quad (5)$$

Here, U is the potential energy of the system, $\eta_{\alpha\beta}$ is the strain, $\alpha, \beta, \kappa,$ and χ are the indices specifying the directions $x, y,$ or $z.$ and i and j are indices specifying the atoms. Furthermore,

$$\Xi_{\alpha\beta}^i = \frac{\partial^2 U}{\partial r_i \partial \eta_{\alpha\beta}}, \quad (6)$$

and

$$H = \frac{\partial^2 U}{\partial r_i \partial r_j}, \quad (7)$$

where r_i is the vector indicating the position of the i -th atom.

Under a small strain, the derivative with respect to strain, $\eta_{\alpha\beta},$ can be obtained by applying the derivative with respect to the interatomic vector defined in the undeformed coordinate, as follows:

$$\frac{\partial U}{\partial \eta_{\alpha\beta}} = \sum_i \sum_{j \neq i} \frac{1}{2} \left(\frac{\partial U}{\partial r_{ij}^\alpha} r_{ij}^\beta + r_{ij}^\alpha \frac{\partial U}{\partial r_{ij}^\beta} \right), \quad (8)$$

where r_{ij} is the vector pointing from atom i to atom j and $r_{ij} = (r_{ij}^x, r_{ij}^y, r_{ij}^z).$ According to this definition, $C_{\alpha\beta\kappa\chi}^{Born}$ is given by

$$\begin{aligned}
C_{\alpha\beta\kappa\chi}^{Born} &= \sum_i^{\square} C_{i,\alpha\beta\kappa\chi}^{born} \\
&= -\frac{1}{4}(\delta_{\alpha\kappa}T_{\beta\chi} + \delta_{\beta\kappa}T_{\alpha\chi} + \delta_{\alpha\chi}T_{\beta\kappa} + \delta_{\beta\chi}T_{\alpha\kappa}) \\
&+ \sum_i^{\square} \sum_{j \neq i}^{\square} \frac{1}{4V} \left(\frac{\partial^2 U}{\partial r_{ij}^\alpha \partial r_{ij}^\kappa} r_{ij}^\beta r_{ij}^\chi + \frac{\partial^2 U}{\partial r_{ij}^\alpha \partial r_{ij}^\chi} r_{ij}^\beta r_{ij}^\kappa + \frac{\partial^2 U}{\partial r_{ij}^\beta \partial r_{ij}^\kappa} r_{ij}^\alpha r_{ij}^\chi \right. \\
&\left. + \frac{\partial^2 U}{\partial r_{ij}^\beta \partial r_{ij}^\chi} r_{ij}^\alpha r_{ij}^\kappa \right), \quad (9)
\end{aligned}$$

where T is the Cauchy stress tensor, defined as follows:

$$T_{\alpha\beta} = \frac{1}{V} \sum_i^{\square} \sum_{j \neq i}^{\square} \frac{\partial U}{\partial r_{ij}^\alpha} r_{ij}^\beta. \quad (10)$$

As described above, the Born term can be expressed as the sum of the contributions from each atom ($C_{i,\alpha\beta\kappa\chi}^{born}$). However, it is difficult to decompose non-affine terms in this manner. This is because the definition of the non-affine term includes the inverse Hessian matrix H . The eigenvalues of the Hessian matrix correspond to the squares of the vibrational mode energies. In solids, Goldstone modes with zero energy appear because of the translational symmetry. This makes the Hessian matrix singular and its inverse ill-defined. Therefore, in the calculation of $C_{\alpha\beta\kappa\chi}^{NA}$, the Hessian matrix with one row and column removed to eliminate the excess degrees of freedom due to translational symmetry is used to evaluate the inverse.⁴⁸ The obtained value of $C_{\alpha\beta\kappa\chi}^{NA}$ is invariant with respect to the choice of fixed atom. However, this treatment is inappropriate when the non-affine term is decomposed into contributions from each atom.

Although it is difficult to decompose the non-affine term, such an analysis is possible for non-affine displacements. The non-affine displacement is defined as follows:

$$(\mathbf{D}_{i,\alpha\beta}^{NA})_k = \frac{\partial r_{ik}}{\partial \eta_{\alpha\beta}} = \sum_{j \neq i}^{\square} \sum_{l=x,y,z}^{\square} (H^{-1})_{ikjl} \frac{\partial^2 U}{\partial r_{jl} \partial \eta_{\alpha\beta}}, \quad (11)$$

The inverse of the Hessian matrix in this equation can be resolved by expanding it using eigenvectors. Letting $\boldsymbol{\psi}_p$ and λ_p be the p -th eigenvector and eigenvalue of the Hessian matrix, respectively, the non-affine displacement can be decomposed as follows:^{3,6}

$$\mathbf{D}_{i,\alpha\beta}^{NA} = \frac{\partial \mathbf{r}_i}{\partial \eta_{\alpha\beta}} = \frac{1}{\lambda_p} \sum_{j \neq i} \sum_p \left(\frac{\partial^2 U}{\partial \mathbf{r}_j \partial \eta_{\alpha\beta}} \cdot \boldsymbol{\psi}_p \right) \boldsymbol{\psi}_p. \quad (12)$$

Molecular dynamics simulation to generate amorphous structures

The structure of amorphous Si was created by using LAMMPS to implement a classical molecular dynamics simulation.⁴⁹ All the molecular dynamics simulations were performed by using an NVT ensemble. The system temperature was controlled by applying a Nosé–Hoover thermostat^{50,51} with a 1-fs time step. The interactions between Si atoms can be described by applying the Stillinger–Weber potential.⁵² Our amorphous Si (a-Si) system model contained $N = 13824$ atoms in a cubic unit cell. The length of each unit cell, $L_x = L_y = L_z = L$, was approximately 65 Å. The resulting mass density of the system was 2.35 g/cm³. The method for creating the amorphous structure followed the procedures described in the literature.^{53–55} First, crystalline Si was heated to 3510 K for 500 ps to melt it into a liquid state. After equilibrating the system at 3510 K for 500 ps, the system was quenched to 10 K at a cooling rate of 10¹¹ K/s. Then, the system was annealed at 100 K for 500 ps following equilibration at 10 K for 500 ps. Subsequently, all atomic velocities were set to zero and structural relaxation was performed. The resulting inherent structure was used as an amorphous model. The shear modulus of the obtained amorphous structure was 33.6 GPa (Born term: 73.7 GPa; non-affine term: 40.1 GPa), which is consistent with previous reports.

For statistical analysis, nine additional independent samples with different initial velocities were created in addition to the main sample analyzed in this study. The average shear modulus of the structures of the 10 samples was 33.2 GPa, with a standard deviation of 0.36 GPa. The averages (standard deviations) of the Born term and non-affine term were 73.5 GPa (0.34 GPa) and 40.3 GPa (0.18 GPa), respectively.

Persistent homology

The HomCloud code^{56,57} was used to apply the persistent homology method, focusing on the first homology. According to convention, we applied the squared values of the radii of the spheres

used in the filtration procedure as the birth and death radii (unit: \AA^2). To identify the optimal ring structure corresponding to each birth–death pair via the inverse analysis, we applied the stable volume⁵⁸ and volume-optimal cycle.⁵⁹ For pairs for which death radius – birth radius > 0.1 , the optimal structure was determined from the stable volume by setting the noise level to 0.001. For other cycles near the diagonal, the optimal structure was determined by using the volume-optimal cycle.

Data Availability

The datasets generated during and/or analyzed during the current study are available from the corresponding author on reasonable request.

Author Contributions

EM conceived the research and performed the simulations in the main text. TN and IO assisted in persistent homology analysis. HM assisted numerical analysis of elastic moduli in amorphous Si. All authors contribute to the discussion, analysis, and writing the manuscript.

Competing Interests

The authors declare they have no competing interests.

Acknowledgments

This study was supported by JST, PRESTO Grant Number JPMJPR2198, and MEXT KAKENHI 21H01816, 23H04470, 22K03543, 23H04495, 19KK0068, 20H05884, and 22H05106, and a grant from the Inamori Foundation.

References

1. Zaccone, A. *Theory of Disordered Solids: From Atomistic Dynamics to Mechanical, Vibrational, and Thermal Properties*. (Springer International Publishing, Cham, Switzerland, 2023).
2. Maloney, C. E. & Lemaître, A. Amorphous systems in athermal, quasistatic shear. *Phys. Rev. E* **74**, 016118 (2006).
3. Lemaître, A. & Maloney, C. Sum Rules for the Quasi-Static and Visco-Elastic Response of Disordered Solids at Zero Temperature. *J. Stat. Phys.* **123**, 415–453 (2006).
4. Zaccone, A., Blundell, J. R. & Terentjev, E. M. Network disorder and nonaffine deformations in marginal solids. *Phys. Rev. B* **84**, 174119 (2011).
5. Grießer, J., Frérot, L., Oldenstaedt, J. A., Müser, M. H. & Pastewka, L. Analytic elastic

- coefficients in molecular calculations: Finite strain, nonaffine displacements, and many-body interatomic potentials. *Phys. Rev. Mater.* **7**, 073603 (2023).
6. Mizuno, H., Mossa, S. & Barrat, J.-L. Measuring spatial distribution of the local elastic modulus in glasses. *Phys. Rev. E* **87**, 042306 (2013).
 7. Demkowicz, M. J. & Argon, A. S. High-density liquidlike component facilitates plastic flow in a model amorphous silicon system. *Phys. Rev. Lett.* **93**, 025505 (2004).
 8. Demkowicz, M. J. & Argon, A. S. Liquidlike atomic environments act as plasticity carriers in amorphous silicon. *Phys. Rev. B* **72**, 245205 (2005).
 9. Argon, A. S. Plastic deformation in metallic glasses. *Acta Metall.* **27**, 47–58 (1979).
 10. Falk, M. L. & Langer, J. S. Dynamics of viscoplastic deformation in amorphous solids. *Phys. Rev. E* **57**, 7192–7205 (1998).
 11. Falk, M. L. & Maloney, C. E. Simulating the mechanical response of amorphous solids using atomistic methods. *Eur. Phys. J. B* **75**, 405–413 (2010).
 12. Ding, J. *et al.* Universal structural parameter to quantitatively predict metallic glass properties. *Nat. Commun.* **7**, 13733 (2016).
 13. Fan, Z., Ding, J., Li, Q.-J. & Ma, E. Correlating the properties of amorphous silicon with its flexibility volume. *Phys. Rev. B Condens. Matter* **95**, 144211 (2017).
 14. Fan, Z., Ding, J. & Ma, E. Machine learning bridges local static structure with multiple properties in metallic glasses. *Mater. Today* **40**, 48–62 (2020).
 15. Bapst, V. *et al.* Unveiling the predictive power of static structure in glassy systems. *Nature Physics* **2020 16:4** **16**, 448–454 (2020).
 16. Cubuk, E. D. *et al.* Identifying structural flow defects in disordered solids using machine-learning methods. *Phys. Rev. Lett.* **114**, 108001 (2015).
 17. Edelsbrunner, H. & Harer, J. *Computational Topology : An Introduction*. (American Mathematical Society, Providence, R.I., 2010).
 18. Zomorodian, A. J. *Topology for Computing*. (Cambridge University Press, 2005).
 19. Elliott, S. R. Medium-range structural order in covalent amorphous solids. *Nature* **354**, 445–452 (1991).
 20. Hiraoka, Y. *et al.* Hierarchical structures of amorphous solids characterized by persistent homology. *Proc. Natl. Acad. Sci. U. S. A.* **113**, 7035–7040 (2016).
 21. Kunii, S., Masuzawa, K., Fogiatto, A. L., Mitsumata, C. & Kotsugi, M. Causal analysis and visualization of magnetization reversal using feature extended landau free energy. *Sci. Rep.* **12**, 19892 (2022).
 22. Sato, R. *et al.* Topological Data analysis of Ion Migration Mechanism. *J. Chem. Phys.* **158**, 144116 (2023).
 23. Nakamura, T., Hiraoka, Y., Hirata, A., Escolar, E. G. & Nishiura, Y. Persistent homology and

- many-body atomic structure for medium-range order in the glass. *Nanotechnology* **26**, 304001 (2015).
24. Onodera, Y. *et al.* Structure and properties of densified silica glass: characterizing the order within disorder. *NPG Asia Materials* **12**, 85 (2020).
 25. Sørensen, S. S., Du, T., Biscio, C. A. N., Fajstrup, L. & Smedskjaer, M. M. Persistent homology: A tool to understand medium-range order glass structure. *Journal of Non-Crystalline Solids: X* **16**, 100123 (2022).
 26. Sørensen, S. S., Biscio, C. A. N., Bauchy, M., Fajstrup, L. & Smedskjaer, M. M. Revealing Hidden Medium-range Order in Amorphous Materials using Topological Data Analysis. *Science Adv.* **6**, eabc2320 (2020).
 27. Minamitani, E., Shiga, T., Kashiwagi, M. & Obayashi, I. Topological descriptor of thermal conductivity in amorphous Si. *J. Chem. Phys.* **156**, 244502 (2022).
 28. Minamitani, E., Obayashi, I., Shimizu, K. & Watanabe, S. Persistent homology-based descriptor for machine-learning potential of amorphous structures. *J. Chem. Phys.* **159**, (2023).
 29. Hong, S. & Kim, D. Medium-range order in amorphous ices revealed by persistent homology. *J. Phys. Condens. Matter* **31**, 455403 (2019).
 30. Murakami, M. *et al.* Ultrahigh-pressure form of Si O₂ glass with dense pyrite-type crystalline homology. *Phys. Rev. B Condens. Matter* **99**, 45153 (2019).
 31. Hirata, A., Wada, T., Obayashi, I. & Hiraoka, Y. Structural changes during glass formation extracted by computational homology with machine learning. *Communications Materials* **1**, 98 (2020).
 32. Shirai, T. & Nakamura, T. Microscopic Description of Yielding in Glass Based on Persistent Homology. *J. Phys. Soc. Jpn.* **88**, 074801 (2019).
 33. Stanifer, E. & Manning, M. L. Avalanche dynamics in sheared athermal particle packings occurs via localized bursts predicted by unstable linear response. *Soft Matter* **18**, 2394–2406 (2022).
 34. Tanguy, A., Mantsi, B. & Tsamados, M. Vibrational modes as a predictor for plasticity in a model glass. *EPL* **90**, 16004 (2010).
 35. Manning, M. L. & Liu, A. J. Vibrational modes identify soft spots in a sheared disordered packing. *Phys. Rev. Lett.* **107**, 108302 (2011).
 36. Rottler, J., Schoenholz, S. S. & Liu, A. J. Predicting plasticity with soft vibrational modes: from dislocations to glasses. *Phys. Rev. E* **89**, 042304 (2014).
 37. Schoenholz, S. S., Liu, A. J., Riggleman, R. A. & Rottler, J. Understanding Plastic Deformation in Thermal Glasses from Single-Soft-Spot Dynamics. *Phys. Rev. X* **4**, 031014 (2014).

38. Gartner, L. & Lerner, E. Nonlinear plastic modes in disordered solids. *Phys Rev E* **93**, 011001 (2016).
39. Richard, D., Kapteijns, G., Giannini, J. A., Manning, M. L. & Lerner, E. Simple and Broadly Applicable Definition of Shear Transformation Zones. *Phys. Rev. Lett.* **126**, 015501 (2021).
40. Kriuchevskiy, I., Sirk, T. W. & Zaccane, A. Predicting plasticity of amorphous solids from instantaneous normal modes. *Phys Rev E* **105**, 055004 (2022).
41. Bonfanti, S., Guerra, R., Mondal, C., Procaccia, I. & Zapperi, S. Elementary plastic events in amorphous silica. *Phys Rev E* **100**, 060602 (2019).
42. Baggioli, M., Kriuchevskiy, I., Sirk, T. W. & Zaccane, A. Plasticity in Amorphous Solids Is Mediated by Topological Defects in the Displacement Field. *Phys. Rev. Lett.* **127**, 015501 (2021).
43. Duan, J., Wang, Y. J., Dai, L. H. & Jiang, M. Q. Elastic interactions of plastic events in strained amorphous solids before yield. *Phys. Rev. Mater.* **7**, 013601 (2023).
44. Wu, Z. W., Chen, Y., Wang, W.-H., Kob, W. & Xu, L. Topology of vibrational modes predicts plastic events in glasses. *Nat. Commun.* **14**, 2955 (2023).
45. Patinet, S., Vandembroucq, D. & Falk, M. L. Connecting Local Yield Stresses with Plastic Activity in Amorphous Solids. *Phys. Rev. Lett.* **117**, 045501 (2016).
46. Cao, Y. *et al.* Structural and topological nature of plasticity in sheared granular materials. *Nat. Commun.* **9**, 2911 (2018).
47. Fan, Z. & Ma, E. Predicting orientation-dependent plastic susceptibility from static structure in amorphous solids via deep learning. *Nat. Commun.* **12**, 1506 (2021).
48. Lutsko, J. F. Generalized expressions for the calculation of elastic constants by computer simulation. *J. Appl. Phys.* **65**, 2991–2997 (1989).
49. Thompson, A. P. *et al.* LAMMPS - a flexible simulation tool for particle-based materials modeling at the atomic, meso, and continuum scales. *Comput. Phys. Commun.* **271**, 108171 (2022).
50. Nosé, S. A unified formulation of the constant temperature molecular dynamics methods. *J. Chem. Phys.* **81**, 511–519 (1984).
51. Hoover, W. G. Canonical dynamics: Equilibrium phase-space distributions. *Phys. Rev. A* **31**, 1695–1697 (1985).
52. Stillinger, F. H. & Weber, T. A. Computer simulation of local order in condensed phases of silicon. *Phys. Rev. B Condens. Matter* **31**, 5262–5271 (1985).
53. Fusco, C., Albaret, T. & Tanguy, A. Role of local order in the small-scale plasticity of model amorphous materials. *Phys. Rev. E* **82**, 066116 (2010).
54. Talati, M., Albaret, T. & Tanguy, A. Atomistic simulations of elastic and plastic properties in amorphous silicon. *EPL* **86**, 66005 (2009).

55. Ishimaru, M., Munetoh, S. & Motooka, T. Generation of amorphous silicon structures by rapid quenching: A molecular-dynamics study. *Phys. Rev. B Condens. Matter* **56**, 15133–15138 (1997).
56. Obayashi, I., Nakamura, T. & Hiraoka, Y. Persistent Homology Analysis for Materials Research and Persistent Homology Software: HomCloud. *J. Phys. Soc. Jpn.* **91**, (2022).
57. HomCloud. <https://homcloud.dev/index.en.html>.
58. Obayashi, I. Stable volumes for persistent homology. *Journal of Applied and Computational Topology* **7**, 671–706 (2023).
59. Obayashi, I. Volume-Optimal Cycle: Tightest Representative Cycle of a Generator in Persistent Homology. *SIAM Journal on Applied Algebra and Geometry* **2**, 508–534 (2018).